Dynamics and fragmentation of small inextensible fibres in turbulence

Sofia Allende, Christophe Henry, Jérémie Bec

PHILOSOPHICAL TRANSACTIONS A

royalsocietypublishing.org/journal/rsta

Research

Cite this article: Allende S, Henry C, Bec J. 2020 Dynamics and fragmentation of small inextensible fibres in turbulence. *Phil. Trans. R. Soc. A* **378**: 20190398.
http://dx.doi.org/10.1098/rsta.2019.0398

Accepted: 27 March 2020

One contribution of 15 to a theme issue 'Fluid dynamics, soft matter and complex systems: recent results and new methods'.

Subject Areas:
fluid mechanics

Keywords:
deformable particles, turbulence, fibres, fragmentation

Author for correspondence:
Jérémie Bec
e-mail: jeremie.bec@mines-paristech.fr

Dynamics and fragmentation of small inextensible fibres in turbulence

Sofía Allende[1], Christophe Henry[2] and Jérémie Bec[1]

[1]MINES ParisTech, PSL Research University, CNRS, CEMEF, Sophia-Antipolis, France
[2]Université Côte d'Azur, INRIA, Team TOSCA, Sophia-Antipolis, France

JB, 0000-0002-3618-5743

The fragmentation of small, brittle, flexible, inextensible fibres is investigated in a fully developed, homogeneous, isotropic turbulent flow. Such small fibres spend most of their time fully stretched and their dynamics follows that of stiff rods. They can then break through tensile failure, i.e. when the tension is higher than a given threshold. Fibres bend when experiencing a strong compression. During these rare and intermittent buckling events, they can break under flexural failure, i.e. when the curvature exceeds a threshold. Fine-scale massive simulations of both the fluid flow and the fibre dynamics are performed to provide statistics on these two fragmentation processes. This gives ingredients for the development of accurate macroscopic models, namely the fragmentation rate and daughter-size distributions, which can be used to predict the time evolution of the fibre size distribution. Evidence is provided for the generic nature of turbulent fragmentation and of the resulting population dynamics. It is indeed shown that the statistics of break-up is fully determined by the probability distribution of Lagrangian fluid velocity gradients. This approach singles out that the only relevant dimensionless parameter is a local flexibility which balances flow stretching to the fibre elastic forces.

This article is part of the theme issue 'Fluid dynamics, soft matter and complex systems: recent results and new methods'.

THE ROYAL SOCIETY PUBLISHING

1. Introduction

The fragmentation process, which consists in breaking a body in different pieces, is very common and relevant to a wide range of phenomena in science and technology [1,2]. Natural examples occurring at different length scales are numerous, from break-up in DNA chains [3,4] to meteors in space [5]. Moreover, a precise understanding of the material properties involved in the breaking process proves fundamental in several industrial applications, as in combustion [6] or in wastewater treatment [7]. Traditionally, fragmentation is modelled from a macroscopic point of view using statistical approaches (e.g. [8–11]) to predict the time evolution of fragment size distributions from empirical observations. It relies on population balance models, which are based on a set of PDEs giving the mean-field behaviour of a population of objects. Such models require information on two quantities: the fragmentation rate (i.e. the frequency of the break-up events) and the daughter size distribution (i.e. the size of all fragments generated by a break-up event). New models for these two quantities are needed to account for the effects of fluctuations and fine physical phenomena occurring during break-up.

We focus here on the fragmentation of brittle elongated particles with a constant length, which will be called inextensible fibres in the following. From the point of view of material sciences, a brittle material breaks under the action of an external force with little elastic deformation and without plastic deformation [12]. In essence, break-up at the molecular level occurs when the local stress overcomes the internal cohesion between molecules. In the case of brittle fragmentation, the fracture induced by this rupture of equilibrium is assumed to propagate instantaneously at the material level leading to the fragmentation of the whole object [10,13]. At the scale of the fibre, this fragmentation can occur due to three different actions: tensile failure occurs when the external force acts to stretch the fibre along its main axis; flexural failure happens when an external torque induces a flexion perpendicular to the fibre main axis; torsional failure occurs when the fibre is twisted by an applied torque. In the present case of brittle materials, we consider the simplest approximation of the fragmentation process where failure happens as soon as a given threshold is reached. In that case, three thresholds are defined for each failure mechanism: a stretch force in tensile failure, a bending angle in flexural failure and a twisting angle in torsional failure. These three thresholds are actually related to each other since they all depend on the material properties and geometry (which govern fragmentation at the molecular level).

This study addresses more specifically the case of inextensible fibres immersed in a fluid. Such situations are found in a number of applications. For example, in the paper industry, cellulose fibres have been investigated in [14]. In a biological context, fibre dynamics have been used to model diatom phytoplankton colonies in the ocean [15] and organic matter at fresh water intakes [16]. Besides, we consider the case of fibres that are smaller compared with the smallest fluid scale (the Kolmogorov scale in turbulent flows). In that case, the dynamics of a fibre is determined by the action of three forces: bending elasticity, viscous drag and internal tension. The fibre will mostly experience tensile and flexural failures due to its stretching or compression by the flow, while torsional failure is negligible due to the fluid flow linearity at such small scales. Bending elasticity and viscous drag act together to stretch the fibre, making it akin to a stiff rod. Tensile failure then occurs when the local tension reaches values above a threshold. However, when fibres change their directions and experience strong-enough compression, their configurations can become buckled [17]: this is known as the buckling instability. The instability has been well documented for simple steady shear flows [18], in which there exists a critical value of the flexibility above which buckling occurs. Clearly, flexural failure can only occur when the fibre buckles and the curvature overcomes a threshold.

The problem of turbulent fragmentation has been essentially addressed for droplets [19,20], fractal flocs [21] and microscopic polymers [22,23]. The break-up of macroscopic fibres has been essentially addressed in laminar flow [24]. Accurate predictions in turbulent flows require extending such work to strongly fluctuating environments and interpreting them within a statistical framework. Remarkably, a similar dynamics holds true for fibres immersed in highly fluctuating environments. For instance, it was shown in [25], that the dynamics of inextensible

Table 1. Numerical and physical parameters of the direct numerical simulation: N^3 number of collocation points, ν kinematic viscosity, Δt time step, $\bar{\varepsilon}$ average kinetic energy dissipation rate, $\eta = \nu^{3/4}/\bar{\varepsilon}^{1/4}$ Kolmogorov dissipative scale, $\tau_\eta = \nu^{1/2}/\bar{\varepsilon}^{1/2}$ Kolmogorov time, $u_{\rm rms}$ root-mean square velocity, $L = u_{\rm rms}^3/\bar{\varepsilon}$ large-eddy length scale, $\tau_L = L/u_{\rm rms}$ large-eddy turnover time, $R_\lambda = \sqrt{15}\, u_{\rm rms}^2/(\nu^{1/2}\bar{\varepsilon}^{1/2})$ Taylor-based Reynolds number.

N^3	ν	Δt	$\bar{\varepsilon}$	η	τ_η	$u_{\rm rms}$	L	τ_L	R_λ
4096^3	10^{-5}	6×10^{-4}	3.8×10^{-3}	7.16×10^{-4}	0.051	0.19	1.86	9.68	731

fibres that are smaller than the Kolmogorov scale in turbulent flow follow most of the time that of stiff rods. Deviations occur when the fibres experience strong-enough local compression, making them buckle. Such events are very rare and intermittent, because of the long-term Lagrangian correlations of turbulent velocity gradients. During these events, the stresses experienced by the particles can be strong enough to lead to their break-up. In fact, turbulent flows are known to generate very large velocity gradients, and those, in turn, may initiate a fragmentation process. Our aim here is to provide such statistics on the mechanisms of fibre break-up in a turbulent flow with dilute fibre suspensions, and specifically to characterize the statistics of the extrema of both the tension and the curvature. Those statistics obtained with fine-scale simulations of individual fibres are used as the basic ingredients, in order to develop accurate macroscopic models, relevant for the above-mentioned natural and industrial applications. Such models predict the time evolution of the fibre size distribution. A question that we want to address relates to the generic nature of turbulent fragmentation processes and of the resulting population dynamics. Turbulent fluctuations are indeed expected to be sufficiently generic to ensure universal behaviours, as for instance observed in [26] for the fragmentation of cracking solids.

To address this problem, we resort to numerical approaches that couple highly resolved turbulent flow simulations to fibre dynamics simulations using the slender-body equation (see below). We focus on the case of inextensible fibres that are brittle, smaller than the Kolmogorov scale and that do not have an effect on the fluid.

This paper is organized as follows. In §2, we give a brief description of our settings, including the slender body theory used to model fibres and the numerical tools used to simulate their dynamics in turbulent flow. We moreover give an overview of the mechanisms pertaining to fibre fragmentation (tensile failure and flexural failure). In §3, we investigate tensile failure and show that it occurs when the fibre is straight. Consequently, the tension is always maximal at its middle and the fibre always breaks in two equal pieces. We also give predictions on the rate at which such failures happen and compare them to numerics. In §4, we turn to flexural failure that happens when the fibre buckles. Thanks to a linear analysis of this instability, we obtain predictions on the associated break-up rates and on the resulting size distribution. Finally, in §5 we summarize our findings and draw some perspectives.

2. Model and numerical method

The objective is to investigate fragmentation processes in a fully developed, homogeneous, isotropic turbulent flow. To that aim, we use direct numerical simulations of the three-dimensional incompressible Navier–Stokes equation. We use the pseudo-spectral solver *LaTu* with 4096^3 collocation points and a third-order Runge–Kutta time marching [27]. A force is added at each time step to keep the kinetic energy constant in the two first Fourier shells. This leads the velocity field to reach a statistically stationary, homogeneous, isotropic turbulent state. The Eulerian parameters of the simulation are summarized in table 1.

Once in a statistical steady state, the flow is seeded with several millions of tracers. Their dynamics is integrated with the same time marching as the fluid and using a cubic interpolation of the velocity field at their location. Their trajectories together with the fluid velocity gradients

at their location are stored with a period $20\Delta t \approx 0.23\,\tau_\eta$ for a time duration of $63\,000\,\Delta t \approx 740\,\tau_\eta \approx 3.9\,\tau_L$). These data are used *a posteriori* to integrate the dynamics of flexible fibres.

We consider very thin fibres that can be approximated as inextensible Euler–Bernoulli beams immersed in a viscous fluid and whose dynamics is thus given by the *local* slender-body theory (e.g. [18]). This model employs fibres with length ℓ and circular cross-section with radius a; the aspect ratio is $\epsilon = a/\ell \ll 1$. The position and conformation of a given fibre is then described by a curve $s \mapsto \mathbf{X}(s,t)$, parametrized by the arc-length coordinate $s \in [-\ell/2, \ell/2]$. We moreover assume that the fibre's inertia is negligible, so that its dynamics is obtained by balancing locally the viscous drag with the fluid to tension and bending elasticity, so that

$$\partial_t \mathbf{X} = \mathbf{u}(\mathbf{X},t) + \frac{1}{\mu}\,\mathbb{D}\left[\partial_s(T\,\partial_s\mathbf{X}) - E\,\partial_s^4\mathbf{X}\right], \quad \text{with } |\partial_s\mathbf{X}|^2 = 1 \tag{2.1}$$

where $$\mu = \frac{8\pi\,\rho_\mathrm{f}\,\nu}{b} \quad \text{and} \quad \mathbb{D} = \mathbb{I} + \partial_s\mathbf{X}\,\partial_s\mathbf{X}^\mathsf{T},$$

where the specific form of the mobility matrix $\mathbb{D}$ arises from the anisotropic drag exerted by the fluid on the slender fibre. This equation is supplemented with the free-end boundary conditions $\partial_s^2\mathbf{X} = 0$ and $\partial_s^3\mathbf{X} = 0$ at $s = \pm\ell/2$. In the above equations, ρ_f is the fluid mass density, E is the fibre's bending modulus (also called flexural rigidity) defined as $E = YI$ (with Y the Young modulus and I the fibre's moment of inertia) and the parameter $b = -\ln(\epsilon^2 e)$ is much larger than 1. The fluid velocity field is denoted by $\mathbf{u}$. We focus on situations where fibres have a very low volume concentration. In this very diluted regime, they are passively transported by the fluid flow, and hence do not influence the dynamics of the advecting velocity field $\mathbf{u}$. The tension, denoted $T(s,t)$, is the Lagrange multiplier associated with the inextensibility constraint $|\partial_s\mathbf{X}|^2 = 1$. The tension is intrinsically non-local. The equation it solves is obtained by requiring that $\partial_t|\partial_s\mathbf{X}|^2 = 0$ and reads

$$\partial_s^2 T - \frac{1}{2}|\partial_s^2\mathbf{X}|^2\,T = 3\,E\,|\partial_s^3\mathbf{X}|^2 + \frac{7}{2}E\,\partial_s^2\mathbf{X}^\mathsf{T}\partial_s^4\mathbf{X} - \frac{\mu}{2}\,\partial_s\mathbf{X}^\mathsf{T}\mathbb{A}(\mathbf{X},t)\,\partial_s\mathbf{X}, \tag{2.2}$$

with the boundary conditions $T = 0$ at $s = \pm\ell/2$. Here $\mathbb{A}$ denotes the velocity gradient $\mathbb{A}_{ij}(\mathbf{X},t) = \partial_j u_i(\mathbf{X},t)$. This equation is equivalent to the Poisson equation satisfied by pressure in incompressible fluid dynamics.

We assume that the fibres have a length ℓ much smaller than the Kolmogorov dissipative scale η. It is easily checked that their centre of mass $\bar{\mathbf{X}}(t)$ then follow the dynamics of simple tracers, namely $\mathrm{d}\bar{\mathbf{X}}/\mathrm{d}t = \mathbf{u}(\bar{\mathbf{X}},t)$. Moreover, the fluid velocity variations along the fibres can be linearized, $\mathbf{u}(\mathbf{X},t) \approx \mathbf{u}(\bar{\mathbf{X}},t) + \mathbb{A}(\bar{\mathbf{X}},t)\,(\mathbf{X} - \bar{\mathbf{X}})$ with a local velocity gradient $\mathbb{A}$ that is constant along the fibre. Under these assumptions, we integrate the local slender-body equation (2.1) along the above-mentioned tracer trajectories, using the finite-difference scheme of [28] with $N = 201$ grid points along the fibre arc-length. The inextensibility constraint is enforced by a penalization method. Time marching uses a semi-implicit Adams–Bashforth scheme with a Lagrangian time step $\Delta t_\mathrm{fib} = 2.5 \times 10^{-5}$. We use a linear interpolation in time to estimate the velocity gradient at a frequency higher than the output from the fluid simulation. Note that the time step required for the fibres is much smaller than that of the fluid. Indeed, we observe that, even by using a semi-implicit scheme, the problem remains particularly stiff when E is small or, equivalently, μ is large. As we will now see, these values of the parameters are of particular relevance.

In addition to the Reynolds number R_λ of the fluid flow, which is prescribed very large, the dynamics of a given fibre depends on a single dimensionless parameter only: the non-dimensional flexibility

$$\mathcal{F} = \frac{8\pi\,\rho_\mathrm{f}\,\nu\,\ell^4}{b\,E\,\tau_\eta}. \tag{2.3}$$

This parameter appears when non-dimensionalizing equation (2.1) with the two relevant scales entering the dynamics and deformation of small fibres, namely their length ℓ and the Kolmogorov dissipative time τ_η. The non-dimensional flexibility can be understood as the ratio between the time scale of the fibre elastic stiffness to that of the turbulent velocity gradients. For small values of $\mathcal{F}$, the fibre is very rigid and behaves as a rod, while for large $\mathcal{F}$, it is very flexible and bends.

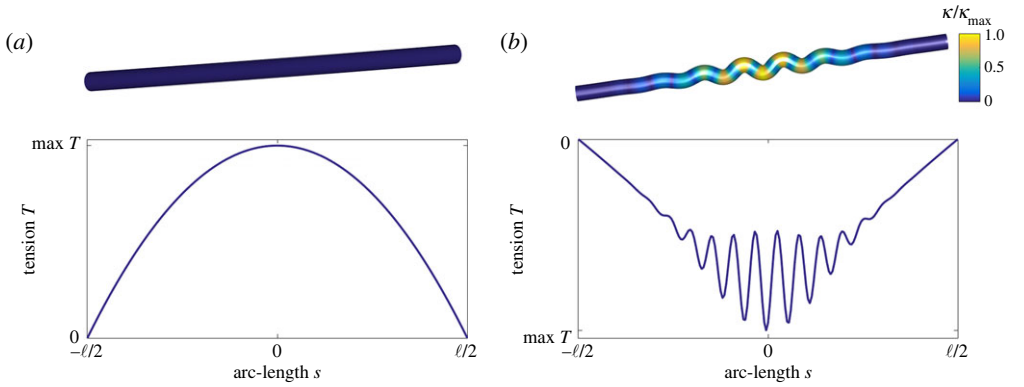

Figure 1. Instantaneous configuration of a fibre with non-dimensional flexibility $\mathcal{F} = 1.6 \times 10^5$ during a buckling event (*b*) and as a stiff rod (*a*). Top: the colour rendering shows the fibre curvature. Bottom: tension as a function of the arc-length at the same instant of time. (Online version in colour.)

In this second case, which corresponds to long fibres (small values of E or large values of μ), the dynamics is much richer and the fibre develop into non-trivial geometrical configurations (see top panels of figure 1).

When the fibre is in a fully straight state (figure 1*a*), one can assume that the tangent vector is constant, i.e. $\partial_s \mathbf{X}(s,t) = \mathbf{p}(t)$ at all values of s. As shown in [28], its direction $\mathbf{p}$ is then a solution of Jeffery's equation for straight inertialess ellipsoidal rods

$$\frac{\mathrm{d}}{\mathrm{d}t}\mathbf{p} = \mathbb{A}\,\mathbf{p} - \dot{\gamma}\,\mathbf{p}, \quad \text{with} \quad \dot{\gamma}(t) = \mathbf{p}^{\mathsf{T}}\mathbb{A}(t)\,\mathbf{p}. \tag{2.4}$$

The orientation $\mathbf{p}$ is sheared and rotated by the velocity gradient tensor $\mathbb{A}$, and the stretching/compression component given by $\dot{\gamma}$ is removed in order to fulfill the constraint $|\mathbf{p}| = 1$. The corresponding term in the right-hand side of (2.4) indeed originates from the tension in the slender-body equation (2.1). The later is obtained by from (2.2) with $\partial_s \mathbf{X} = \mathbf{p}$, leading to

$$T(s,t) = -\frac{\mu}{4}\,\dot{\gamma}(t)\left(s^2 - \frac{\ell^2}{4}\right), \tag{2.5}$$

meaning that the tension is maximal in the middle of the fibre and follows a parabolic shape with the arc-length coordinate s (figure 1*a*). When the fibre is strongly compressed ($\dot{\gamma} < 0$), the straight configuration might become unstable, leading to buckling (figure 1*b*). In that case, the tension can display several local extrema (this will be discussed later in §a).

In turbulence, fibres are most of the time in a straight state and very rarely buckle [25]. It was shown there that the buckling instability develops when the instantaneous value of $\dot{\gamma}$ takes large negative values. Besides, velocity gradients in turbulent flows can experience arbitrarily large fluctuations. This impacts the dynamics of the fibre, and in particular the transition rates between the straight and the buckled configurations. Explicitly, the fibres behave as stiff rods in calm regions, and fibres bend/stretch more frequently in very fluctuating regions.

Large turbulent fluctuations may then initiate a break-up process. Indeed, strong stretching and compression by the flow produces large values of the tension and curvature, respectively. As anticipated, two mechanisms can then initiate a fragmentation: *tensile failure* when the fibre breaks because the local tension is too high, and *flexural failure* when the fibre breaks due its curvature being too large. Large positive values of the tension leading to tensile failure are attained when the fibre is in a fully straight configuration and experiences a strong shear from the flow, as shown in figure 1*a*. In this configuration, the bending energy is zero, thus the tension balance the stretching due to velocity gradients. The solution of the tension is then a parabola, where the maximum is attained in the middle of the fibre—as transpires from equation (2.5).

Conversely, as is illustrated on the top panel of figure 1*b*, the curvature becomes very large during buckling. Such large values of the curvature could lead to fragmentation through flexural failure. These instabilities are typically dominated by a single mode with symmetric properties. Such modes depends on the flexibility of the fibre and on the magnitude of the compression by the flow. Depending on which of these two mechanisms is predominant, the fibres might break at different locations. This could imply very different evolutions of the distribution evolution of the fibre size distribution [29].

3. Fragmentation through tensile failure

We here start by investigating fragmentation due to large values of the tension. This occurs when the maximal tension along the fibre is larger than a critical value $T^\star$ that depends on its material properties. To estimate the contribution of this mechanism to the fragmentation process, we need to study both the rate $\lambda_T(T^\star)$ at which a large tension is attained and the location where the maximum is located on the fibre.

Large tensions are reached when the fibre experiences a strong stretching along its main axis and is thus generally in a fully straight state. In that case, we have seen in the previous section (cf. equation (2.5)) that the tension is a concave parabola with its maximum

$$T_{\max} = \frac{\mu\,\dot\gamma\,\ell^2}{16}, \tag{3.1}$$

reached at the middle of the fibre. As a consequence, a tensile failure will always break short fibres in two equal pieces, giving a trivial daughter distribution. It should be noted here that this is true for fibres without molecular defects (i.e. $T^\star$ is constant along the fibre length).

Another consequence is that tensile failure occurs when the stretching rate along the fibre exceeds a critical value, namely $\dot\gamma > 16\,T^\star/(\mu\ell^2)$, and thus when the velocity gradient reaches strong positive values. Turbulent gradients along the Lagrangian path are known to display very sharp fluctuations and oscillations. This implies that the rate at which a large value of $\dot\gamma$ is exceeded, is approximately proportional to the probability distribution at this value, so that

$$\lambda_T(T^\star) \propto \Pr\left(\dot\gamma > \frac{16\,T^\star}{(\mu\ell^2)}\right). \tag{3.2}$$

The right-hand side involves the distribution of $\dot\gamma$ and thus that of fluid velocity gradients. In large-Reynolds-number turbulence, this distribution is fairly approximated by a lognormal with far tails which are actually closer to a stretched exponential with an exponent $\approx 1/2$—e.g. [30–33]). Either of these two behaviours are compatible with our observations: For large values of the tension it is not possible to distinguish one from the other. The inset of figure 2 shows the probability density function of the stretching rate $\dot\gamma$. Its behaviour at positive values is well represented by a lognormal distribution when $\dot\gamma$ is of the order of τ_η^{-1} with a far tail at $\dot\gamma \gg \tau_\eta^{-1}$ that rather approach a stretched exponential behaviour. As stressed in [34], the coefficients used in fits have a non-trivial dependence upon the Reynolds number. From now on, we focus on the case $R_\lambda = 731$, as chosen in our simulation. We will come back to this dependence in the conclusions.

These considerations suggest to use these two possibles forms to fit the tensile fragmentation rate λ_T as a function of the physical parameters of the fibre. When $T^\star/(\mu\ell^2) \gg \tau_\eta^{-1}$, a stretched-exponential form is expected to be more relevant, so that

$$\lambda_T(T^\star) \approx \lambda_0\,\exp\left[-a\left(\frac{\tau_\eta\,T^\star}{\mu\ell^2}\right)^{1/2}\right], \tag{3.3}$$

with fitting parameters a frequency, λ_0, and a dimensionless constant a. As can be seen in figure 2, such a formula gives indeed a good approximation to numerical calculations of the tensile fragmentation rates.

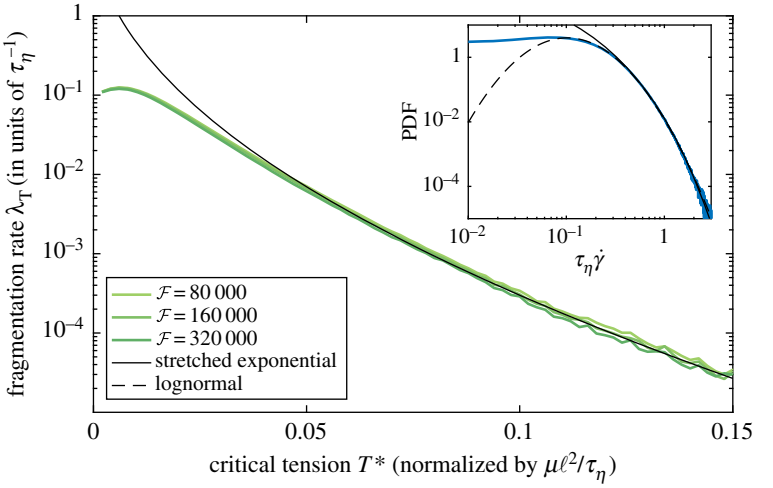

Figure 2. Tensile fragmentation rate λ_T as a function of the critical tension $T^\star$ for various values of the non-dimensional flexibility $\mathcal{F}$. The rate has been non-dimensionalized by τ_η^{-1} while the x axis displays $\tau_\eta\, T^\star/(\mu\ell^2)$. The solid line is the stretched-exponential fit (3.3) with $\lambda_0 = 14\,/\tau_\eta$, $a = 34$ and $\tau \approx \tau_\eta$. The dashed line is the lognormal fit (3.4) with $\lambda_0' = 0.13/\tau_\eta$, $a' = 1.12$ and $\tau = 102\,\tau_\eta$. Inset: Probability density function (PDF) of the stretching rate $\dot{\gamma}$ at positive values (blue bold solid line, blue online), together with a stretched exponential fit (thin line) and a lognormal fit (dashed line). (Online version in colour.)

At $T^\star/(\mu\ell^2) \sim \tau_\eta^{-1}$, as can be seen in figure 2, the tensile fragmentation rate behaves as a lognormal, namely

$$\lambda_T(T^\star) \approx \lambda_0' \exp\left[-a'\left(\log\frac{\tau\, T^\star}{\mu\ell^2}\right)^2\right], \tag{3.4}$$

where a' is a dimensionless fitting constant, and λ_0' and τ are fitting parameters with dimensions of a frequency and a time, respectively. The values of these parameters reported in the caption suggest that, while λ_0' is of the order of the Kolmogorov time scale τ_η, the time τ is 100 times larger. This can be explained by the fact that $T_{\max}(\mu\ell^2) \sim \dot{\gamma}/16$ and in turn, as seen in [25], typical values of $\dot{\gamma}$ are of the order of $0.1/\tau_\eta$ leading to a factor of the order of 100.

To summarize this section, let us stress that tensile failure is here entirely prescribed by the (intermittent) statistics of the velocity gradients. This is a stylized feature of our approach, and provides a simplified framework to study fragmentation. Note that this assumption holds true only for small fibres. When considering fibres larger than the Kolmogorov length scale, the velocity gradient will not be uniform along the fibre. This implies in particular that the fibre could be locally stretched and compressed at the same time and breaks in pieces of arbitrary sizes.

Also, it is important to notice that reaching large values of the tension requires $\dot{\gamma}$ to locally exceed a critical value that is $\propto \ell^{-2}$. Tensile failure thus becomes rarer and rarer when fibres become smaller. In addition, the daughter population is typically centred over the half of the mother size. This implies that a fragmentation process involving only tensile failure cannot efficiently lead to the fast formation of small fragments. As we will see in the next section, this strongly differs when flexural failure is involved. In that case, many small segments can be created during a single event.

4. Fragmentation through flexural failure

Conversely to tensile failure, flexural failure displays a much more complicated behaviour. Such break-ups happen when the fibre is bent and, more precisely, when the curvature becomes larger than a given threshold. Then, there exists a location s along the fibre such that, at the

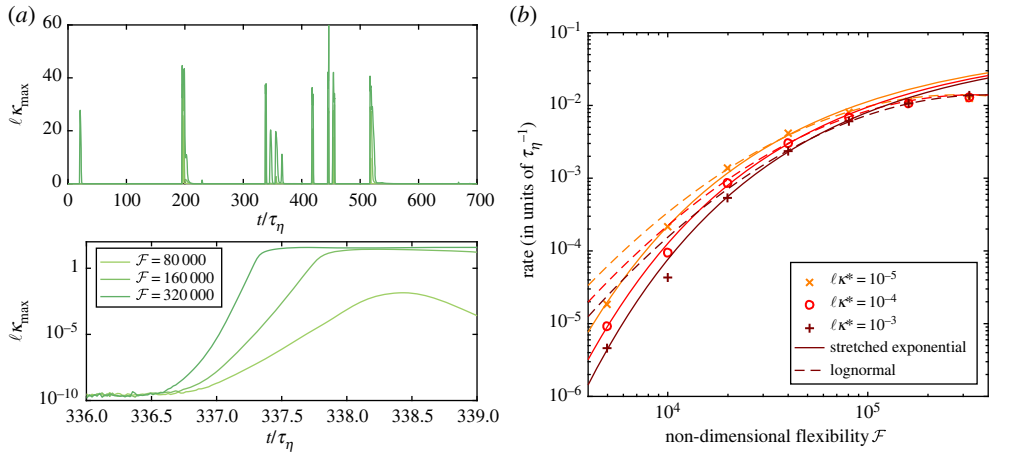

Figure 3. (*a*) Time evolution of the maximal curvature $\kappa_{\max}$ along a single turbulent tracer trajectory but for three different values of the non-dimensional flexibility $\mathcal{F}$. The upper part shows the full trajectory, while the lower is a semilogarithmic time zoom on the buckling event occurring at time $t \approx 337\ \tau_\eta$. (*b*) Rates at which the maximal curvature exceeds given values $\kappa^\star$ (as labelled) as a function of the non-dimensional flexibility. Each dataset is fitted by both a stretched exponential (solid curves) and by a lognormal (dashed curves). (Online version in colour.)

break-up time $t^\star$, one has $|\partial_s^2 \mathbf{X}(s, t^\star)| \geq \kappa^\star$. Clearly, as the curvature is continuous with respect to arc-length and time, such a break-up occurs at the first time when the maximum of curvature $\kappa_{\max} = \max_s |\partial_s^2 \mathbf{X}|$ exceeds $\kappa^\star$. As anticipated in §2, these events happen when the fibre undergo a buckling. Such an instability occurs when the instantaneous value of the stretching rate $\dot{\gamma}$ defined in equation (2.4) becomes large negative (compression). Figure 3*a* shows the time evolution of the fibre's maximal curvature along a Lagrangian trajectory for different values of $\mathcal{F}$. It can be seen that buckling events, for which $\kappa_{\max} \neq 0$, are very sparse and intermittent. Such events are separated by long periods, which can be of the order of the large-eddy turnover time, during which the fibre is fully straight, up to numerical precision. It is shown in [25] that in turbulence, the rate at which buckling appears is similar to an activation process. More precisely, it was found that the fibre buckles when its instantaneous flexibility $\mathcal{F}_{\text{loc}}(t) = \tau_\eta\, |\dot{\gamma}(t)|\, \mathcal{F}$ becomes larger than a critical value $\mathcal{F}^\star$, provided that $\dot{\gamma}(t) < 0$. This leads to estimate the buckling rate as

$$\lambda_{\text{Buckl}} \propto \Pr\left(\dot{\gamma} < -\frac{\mathcal{F}^\star}{(\tau_\eta\, \mathcal{F})}\right). \tag{4.1}$$

As in the case of tensile failure rates, the distribution of the stretching rate $\dot{\gamma}$ can be approximated either by a lognormal or by a stretched exponential, leading to approximations of the above formula. We expect the rate of flexural failure to be upper bounded by this buckling rate.

However, for break-up to occur, we additionally require that the maximum curvature exceeds $\kappa^\star$. The corresponding rates are shown in figure 3*b* as a function of the non-dimensional flexibility $\mathcal{F}$ and for various values of the threshold $\kappa^\star$. Lognormal and stretched exponential functional forms give good approximations with fitting parameters that depend on $\kappa^\star$. Understanding this dependence requires investigating more closely the development of the instability. Figure 3*c* shows the time growth of the maximum of curvature during one of these events for various values of the non-dimensional flexibility. One observes that the increase is approximately exponential with a rate that depends on $\mathcal{F}$. Small values of $\kappa^\star$ are reached during the instability growth and it is thus needed to characterize further this regime in order to quantify how this affect rates. The development of the buckling instability is furthermore of importance as flexural failure will actually not happen when the threshold is exceeded but rather when it is for the first time. At difference with tension that has fast fluctuations, the curvature has an on–off behaviour.

As can be seen in figure 3*c*, the growth of $\kappa_{\max}$ can be followed by a period during which it remains at finite values for quite some time. This indicates that the rates shown in figure 3*b* are actually overestimating the actual flexural failure rates. In the following, we provide more accurate estimates.

(a) Linear analysis and relevance to turbulent flows

The buckling instability occurs when the fibre, initially in a straight configuration $\partial_s \mathbf{X} \equiv \mathbf{p}$, experiences a strong compression by the flow. This is likely to happen when the flow locally displays a violent shear, so that the rodlike fibre is like a Jeffery orbit [35]: in that case, the rod rotates and is not aligned with the flow. During such event, the fibre alternatively experience stretching and compression along its main axis, giving it the opportunity to buckle. Performing a linear stability analysis for such orbits is however complex. Indeed, upon buckling, the initially straight fibre picks a specific trajectory among an infinite family. The selected trajectory depends on the initial perturbation and is very sensitive to fine sub-leading details, such as thermal noise [36], fibre or fluid inertia [37,38], or, as in our turbulent settings, the fact that the flow is not a pure shear.

As we will see in the sequel, a simplified linear stability analysis already fairly describes buckling events, meaning that we can avoid delving into the complicated context of Jeffery orbits. Let us consider that the fibre experiences a time-constant compression $\dot{\gamma} = \mathbf{p}^{\mathsf{T}} \mathbb{A}\, \mathbf{p} < 0$ along its direction. The base solution $\mathbf{p}(t)$ describes a rod-like solution to the slender body equation (2.1). We introduce a perturbed solution as $\mathbf{X}(s,t) = \bar{\mathbf{X}}(t) + s\,\mathbf{p}(t) + \boldsymbol{\chi}(s,t)$, where $\bar{\mathbf{X}}(t)$ is the average position of the fibre centre of mass and the perturbation $\boldsymbol{\chi}$ is of small amplitude (i.e. $|\boldsymbol{\chi}| \ll \ell$). For buckling, we are interested in perturbations that grow perpendicularly to the fibre direction. The two transverse components of $\boldsymbol{\chi}$ are decoupled and evolve as (e.g. [18])

$$\frac{1}{|\dot{\gamma}|}\,\partial_t \chi = \chi + s\,\partial_s \chi + \frac{1}{4}\left(s^2 - \frac{\ell^2}{4}\right)\partial_s^2 \chi - \frac{E}{\mu\,|\dot{\gamma}|}\,\partial_s^4 \chi, \tag{4.2}$$

with the free-end boundary conditions $\partial_s^2 \chi = 0$ and $\partial_s^3 \chi = 0$ at $s = \pm \ell/2$. This linear equation admits solutions of the form $\chi(s,t) = \mathrm{e}^{\rho\, t}\, \hat{\chi}(s)$, where $\hat{\chi}$ is the eigenfunction of the right-hand side of (4.2) associated with the eigenvalue ρ. Once time is rescaled by $\dot{\gamma}^{-1}$ and arc-length by ℓ, this eigenvalue problem depends on a unique non-dimensional parameter $\mathcal{F}_{\mathrm{loc}} = \mu\,|\dot{\gamma}|\,\ell^4/E$, which measures the ratio between the fluid compression and the elastic force. Because of the presence of non-constant coefficients, there is no straightforward way to obtain the full spectrum of eigenmodes as a function of the dimensionless flexibility $\mathcal{F}_{\mathrm{loc}}$. Still, there are two trivial solutions given by $\rho/\dot{\gamma} = 1$ with $\hat{\chi} = \text{const.}$ and $\rho/\dot{\gamma} = 2$ with $\hat{\chi} = a\,s$ and a constant. For these two unstable modes, the fibre remains straight and does not buckle. To access more complicated configurations, we rely on integrating numerically equation (4.2).

Figure 4*a* represents the 30 most unstable eigenvalues as a function of the non-dimensional flexibility. A first non-straight mode becomes unstable when $\mathcal{F}_{\mathrm{loc}} > \mathcal{F}_1^\star \approx 153$. This threshold is in agreement with [18]. This first growing mode, labelled as $n = 1$, is shown in figure 4*b*. When $\mathcal{F}_{\mathrm{loc}}$ increases, there is a sequence of bifurcations with a change of the most unstable eigenfunction. We label these modes with the number n of extrema that $\hat{\chi}$ contains (see panel *b*). The first bifurcation is between order $n = 1$ and $n = 2$, which occurs at $\mathcal{F}_{\mathrm{loc}} = \mathcal{F}_2^\star \approx 1840$. When $\mathcal{F}_{\mathrm{loc}}$ further increases, the most unstable modes are of higher order n. It also appears from figure 4*b* that the amplitude of fluctuations decreases very fast as the arc-length coordinate s gets further from the fibre centre. One finally observes that when $\mathcal{F}_{\mathrm{loc}} \to \infty$, the most unstable eigenvalues grow as $\rho/\dot{\gamma} \propto \mathcal{F}_{\mathrm{loc}}$.

In this asymptotics of large dimensionless flexibility, the small parameter $\mathcal{F}_{\mathrm{loc}}^{-1}$ multiplies the highest-order derivatives. This indicates that the limit is singular but could actually be tackled using a WKB (Wentzel, Kramers, Brillouin) perturbative approach (e.g. [39]). The WKB method

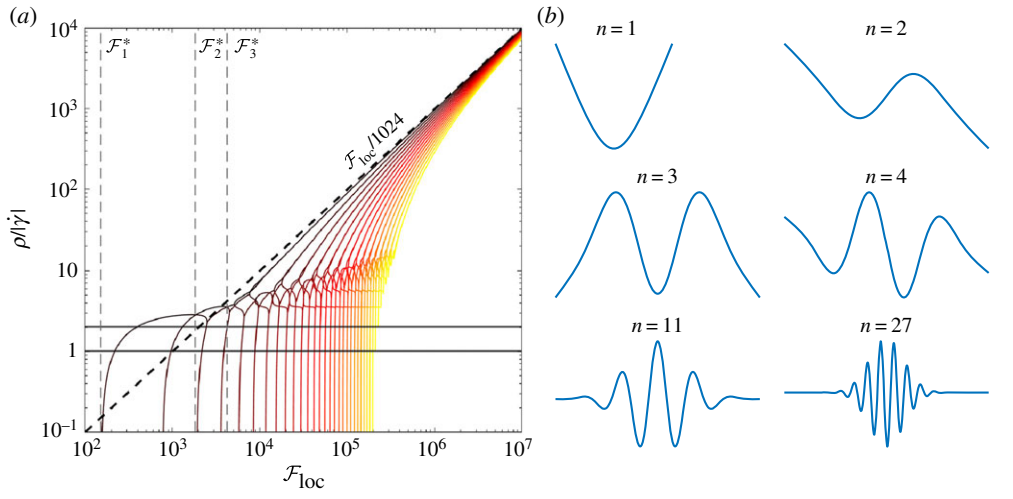

Figure 4. (*a*) Thirty largest eigenvalues associated with the linear evolution (4.2) as a function of $\mathcal{F}_{\rm loc}$. The two horizontal lines at $\rho=\dot\gamma$ and $\rho=2\dot\gamma$ show the two unstable straight modes. The three vertical lines at $\mathcal{F}_{\rm loc}=\mathcal{F}_1^\star$, $\mathcal{F}_2^\star$ and $\mathcal{F}_3^\star$ are bifurcations above which the most unstable non-straight mode is $n=1$, 2 and 3, respectively. The dashed line represents the asymptotic behaviour $\rho/\dot\gamma\simeq\mathcal{F}_{\rm loc}/1024$ reached at large values. (*b*) Illustrations of the fibre geometric state in eigenmodes of various orders n. (Online version in colour.)

suggests writing the solution as the exponential of an asymptotic series expansion

$$\hat\chi(s)\sim\exp\left(\frac{1}{\varepsilon}\sum_{p\geq0}\varepsilon^p\varphi_p(s)\right), \tag{4.3}$$

where $\varepsilon=\mathcal{F}_{\rm loc}^{-\delta}$ is a small parameter and $\varphi_p(s)$ are terms in the expansion. The exponent $\delta>0$ is obtained by substituting the expansion (4.3) in (4.2) and balancing the leading-order terms. Far from the fibre's ends, one has

$$\frac{\rho}{|\dot\gamma|}=\frac{1}{4\,\varepsilon^2}\left(s'^2-\frac{1}{4}\right)(\partial_{s'}\varphi_0)^2-\frac{1}{\mathcal{F}_{\rm loc}\,\varepsilon^4}\,(\partial_{s'}\varphi_0)^4, \tag{4.4}$$

with $s'=s/\ell$. This gives $\varepsilon=\mathcal{F}_{\rm loc}^{-1/2}$ and $\rho/|\dot\gamma|\sim\mathcal{F}_{\rm loc}$, meaning that $\delta=1/2$ and confirming the observed linear behaviour of the eigenvalues in the asymptotics of $\mathcal{F}_{\rm loc}\to\infty$. Besides, when $\mathcal{F}_{\rm loc}$ increases, the order n of the dominant mode becomes larger and the eigenfunction gets more localized at $|s'|\ll1$. This suggests expressing the dominant term as $\varphi_0(s')=a_0+a_1\,s'+a_2\,s'^2+a_3\,s'^3+\cdots$. Now, using this expansion in (4.4) and balancing equal powers of s', one obtains to leading order

$$\frac{\rho}{|\dot\gamma|}=-\frac{\mathcal{F}_{\rm loc}}{16}\,a_1^2-\mathcal{F}_{\rm loc}\,a_1^4,\quad\text{so that } a_1^2=-\frac{1}{32}\pm\sqrt{\frac{1}{1024}-\frac{\rho}{|\dot\gamma|\,\mathcal{F}_{\rm loc}}}. \tag{4.5}$$

This leading term contributes an exponential behaviour $\propto\exp(\pm\sqrt{\mathcal{F}_{\rm loc}}\,a_1)$ at $s'=\pm1$ in the eigenfunction $\hat\chi$. When the real part of b is non-zero, this term diverges as a function of $\mathcal{F}_{\rm loc}$ and this is incompatible with the imposed free-end boundary conditions. a_1 should thus be a pure imaginary number. This means that a_1^2 is real negative, and with (4.5), we get necessarily $\rho/\dot\gamma<\mathcal{F}_{\rm loc}/1024$, the maximal eigenvalue corresponding to the case when the bound is reached. This prediction gives the value 1/1024 for the constant of the linear behaviour of ρ, in agreement with the measurements reported in figure 4. Note that for this specific eigenvalue, one obtains $a_1=\mathrm{i}/\sqrt{32}$ (i being the imaginary unit).

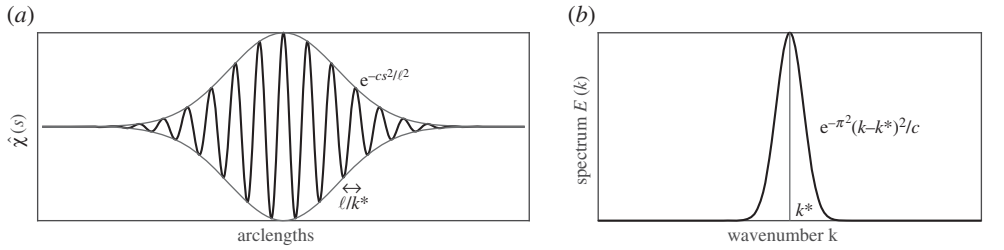

Figure 5. (*a*) Typical asymptotic shape of the eigenfunctions consisting of a fast oscillation with a Gaussian envelope. (*b*) Spectrum $E(k) = |\mathbb{F}[\hat{\chi}](k)|^2$ of the same function, where $\mathbb{F}[\hat{\chi}]$ designates the Fourier transform of $\hat{\chi}$. It is a Gaussian centred at $k = k^\star$ with variance $c/(2\pi^2)$.

Moving on to higher-order terms, one can easily check that contributions of the order of s' vanish for the above value of a_1. As to the terms $\propto s'^2$, they give

$$0 = \frac{1}{4}a_1^2 - \frac{1}{16}(4\,a_2^2 + 6\,a_1 a_3) - \left(24\,a_1^2 a_2^2 + 12\,a_1^3 a_3\right). \tag{4.6}$$

Using $a_1 = \mathrm{i}/\sqrt{32}$, we get $a_2 = -1/8$. This finally leads to writing $\varphi_0 \approx a_0 + \mathrm{i}\,s'/\sqrt{32} - s'^2/8$.

This asymptotic analysis suggest to write the eigenfunction of order n as

$$\hat{\chi}(s) = \begin{cases} \mathrm{e}^{-c\,(s/\ell)^2}\cos(2\pi\,k^\star\,s/\ell) & \text{for } n = 2\,k^\star + 1 \text{ odd}, \\ \mathrm{e}^{-c\,(s/\ell)^2}\sin(2\pi\,k^\star\,s/\ell) & \text{for } n = 2\,k^\star \text{ even}, \end{cases} \tag{4.7}$$

whose typical shape is represented in figure 5*a*. The above asymptotic analysis shows that the most unstable mode is characterized by an oscillating function with a wavelength $k^\star$ and a Gaussian envelope with a coefficient c. These two parameters are given by

$$k^\star \simeq \frac{\sqrt{\mathcal{F}_{\mathrm{loc}}}}{2\pi\sqrt{32}} \quad \text{and} \quad c \simeq \frac{\sqrt{\mathcal{F}_{\mathrm{loc}}}}{8}. \tag{4.8}$$

To estimate numerically $k^\star$ and c, we use the Fourier spectrum of the eigenfunction. It is defined as the squared modulus of the coefficients of the Fourier transform of $\hat{\chi}$. As illustrated in figure 5*b*, the spectrum of the asymptotic form (4.7) is a Gaussian function of k. The wavenumber $k^\star$ is approximated as the mean associated with this distribution, while the coefficient c is deduced from its variance. We use this approach to measure $k^\star$ and c as a function of $\mathcal{F}_{\mathrm{loc}}$ for the eigenfunctions obtained numerically from the integration of the linear system (4.2). The results are displayed as solid curves on figure 6, together with the asymptotic predictions (4.8) displayed as black dashed curves. The good agreement between these curves confirm the relevance of the asymptotic analysis at large values of $\mathcal{F}_{\mathrm{loc}}$ that we consider here.

Following this linear analysis, we then perform the same kind of analysis to the case of fibres that follow turbulent trajectories. To capture the dawn of the instability, we track fibres whose curvature, after having almost relaxed to zero, grows again and exceeds a given threshold. We use the fibre's shape at the instant of time when the threshold is first reached as an estimate of the growing mode. In such fluctuating settings, we make use of the instantaneous non-dimensional flexibility $\mathcal{F}_{\mathrm{loc}} = \tau_\eta|\dot{\gamma}|\,\mathcal{F}$. For each event, we measure $k^\star$ and c from the Fourier spectrum of the fibre shape. We then compute their average value conditioned on the observed value of $\mathcal{F}_{\mathrm{loc}}$. The resulting estimates are shown as symbols in figure 6 for three different values of $\mathcal{F}$. Clearly, these measurements show that the linear analysis reported above is able to describe the growth of buckling modes in turbulent flows, assuming that the relevant parameter is given by the instantaneous value of the non-dimensional flexibility.

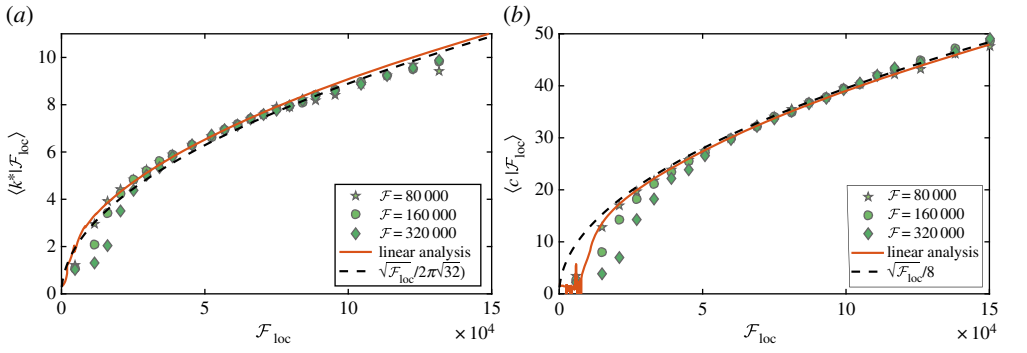

Figure 6. Numerical estimates of the wavenumber $k^\star$ (*a*) and of the coefficient c of the Gaussian envelope (*b*) characterizing the most unstable mode. Results are shown both for the numerical integration of the linearized dynamics (solid curves) and for turbulent data (symbols associated with various $\mathcal{F}$, as labelled). The asymptotic predictions (4.8) are shown as black dashed curves. (Online version in colour.)

(b) Estimates for flexural fragmentation rates in turbulence

We now apply the above considerations to determine both the rate at which flexural failure occurs and the resulting daughter size distribution upon fragmentation. We assume that the fibres are brittle, so that they break as soon as their curvature exceeds a critical value $\kappa^\star$, which is relatively small. Because of that, break-up happens while the fibre is still at the beginning of a buckling event that can be described within the linear approximation. We moreover assume that the instability growth is given by eigenvalues and eigenfunctions that are properly described by the large-flexibility asymptotics of the previous subsection (this assumption is only valid if the growth rate is large enough to consider that the shear $\dot\gamma$ is constant during the instability and so $\mathcal{F}$ is large).

(i) Fragmentation rate

The rate at which flexural failure occurs is the rate at which the maximal curvature along a fibre exceeds for the first time the critical value $\kappa^\star$. A first condition for this to happen is to have the fibre developing a buckling: this requires $\mathcal{F}_{\rm loc} = \tau_\eta\,|\dot\gamma|\,\mathcal{F}$ becoming larger than a critical value $\mathcal{F}^\star$ at time t_0, which marks the beginning of the event. After that, the instability grows exponentially with a rate $\rho \simeq |\dot\gamma|\,\mathcal{F}_{\rm loc}/1024$. The maximal curvature also follows this growth, so that

$$\kappa_{\max}(t) \simeq \kappa_{\max}(t_0)\,\exp\left[\frac{\tau_\eta\,|\dot\gamma|^2\,\mathcal{F}}{1024}\,(t-t_0)\right]. \tag{4.9}$$

Of course, without an initial curvature nothing would happen. It is indeed required to have initially a small deviation to the base state for the instability to develop. In physical situations, several effects give such perturbations, including thermal noise, material inhomogeneities along the fibres, a small extensibility, the fluid flow modifications due to the fibre, and more importantly, the sub-leading turbulent fluctuations that are neglected when we assume that the fibre samples a space-independent fluid velocity gradient. Such effects are clearly not in the model we use. Still, in our simulations, the instability is triggered by a small numerical noise that comes either from the accuracy of the method, from roundoff errors, or from the penalty approach that is used to enforce inextensibility. This error is visible in figure 3*c* where, before the buckling starts, one has $\kappa_{\max} \approx \kappa_0 \approx 2\times 10^{-10}\,\ell^{-1}$.

No matter how small they are, arbitrary values of curvature are not necessarily reached by all buckling events. For instance, during the specific event shown in figure 3*c*, the maximal curvature barely reaches $\kappa_{\max} = 10^{-2}\,\ell^{-1}$ in the case of the fibre with the smallest flexibility. The growth rate

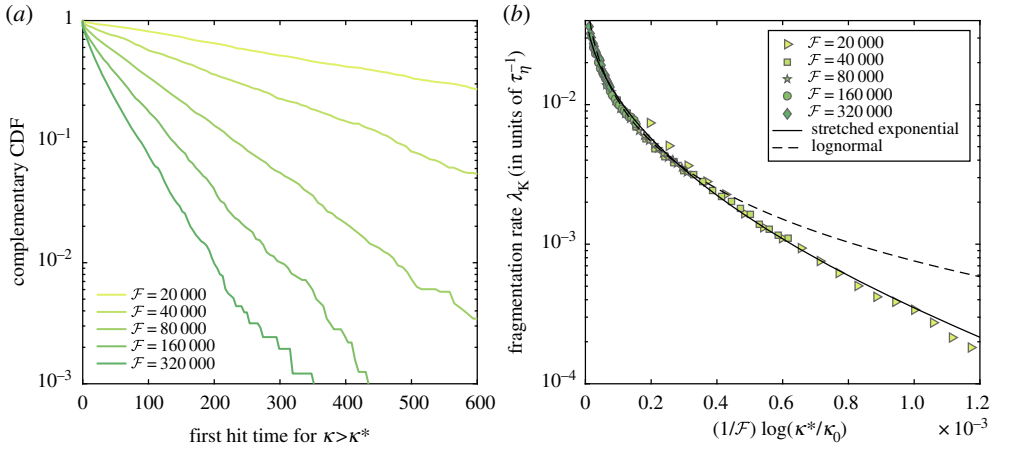

Figure 7. (*a*) Complementary Cumulative Distribution Function (CDF) of the first time at which the fibres curvature hits a value $\kappa^\star = 10^{-6}$, shown for various values of the flexibility, as labelled. (Time is here in units of τ_η.) (*b*) Fragmentation rate λ_K as a function of the dimensionless parameter $(1/\mathcal{F})\ \log(\kappa^\star/\kappa_0)$, with a reference curvature set to $\kappa_0 = 2 \times 10^{-10}$. Symbols correspond to different values of $\kappa^\star$ and $\mathcal{F}$. The solid line is the stretched-exponential fit (4.12) with $\lambda_0 = 0.055\ \tau_\eta^{-1}$ and $a = 160$. The dashed line is the lognormal fit (4.13) with $\lambda_0' = 0.06\ \tau_\eta^{-1}$, $a' = 0.11$, and $b' = 13.12$. (Online version in colour.)

is there too small or, equivalently, compression does not last long enough. During this very event, the two other more flexible fibres reach much larger curvatures and saturate at $\kappa_{\max} \approx 30\ell^{-1}$. These distinct behaviours originate from large differences in the instability growth rates. The time during which the fibre is compressed is completely determined, either by the fluid flow through the Lagrangian persistence time of velocity gradients, or by the evolution of the base orientation $\mathbf{p}(t)$, which for instance perform a Jeffery orbit and tumbles. In both cases, the relevant time scale during which the fibre is compressed is of the order of $|\dot\gamma|^{-1}$.

A necessary condition for the fibre to break is thus that it reaches curvatures larger than $\kappa^\star$ on a time smaller than the compression duration $\simeq \alpha\,|\dot\gamma|^{-1}$, where α is an order-unity constant. Using the exponential law (4.9), one should thus have

$$t - t_0 \simeq \frac{1024}{\tau_\eta\,|\dot\gamma|^2\,\mathcal{F}}\ \log\left(\frac{\kappa^\star}{\kappa_0}\right) < \alpha\,|\dot\gamma|^{-1}. \tag{4.10}$$

This leads to the following estimate for the rate at which flexural failure occurs:

$$\lambda_K(\kappa^\star) \propto \Pr\left(\dot\gamma < -\frac{[(1024/\alpha)\ \log(\kappa^\star/\kappa_0)]}{(\tau_\eta\,\mathcal{F})}\right). \tag{4.11}$$

This formula is similar to the buckling rate of equation (4.1) except that, this time, the critical non-dimensional flexibility depends on $\kappa^\star$. Also, it suggests that λ_K is simply a function of the dimensionless parameter $(1/\mathcal{F})\ \log(\kappa^\star/\kappa_0)$ that can be fitted, as before, by either a stretched exponential or a lognormal.

To test this prediction numerically, the main difficulty is to estimate this rate from finite-time simulations. Depending on the values of the fibre flexibility and of the critical curvature, the typical time needed for the curvature to become larger than $\kappa^\star$ can be longer than the simulation duration. Hence, to estimate this rate, we have rather measured the probability distribution of the first time at which $\kappa_{\max}$ hits $\kappa^\star$. The complementary cumulative distribution function is shown in figure 7*a* for different flexibilities and a fixed value of the critical curvature. Clearly, one observes that the first-hit time follows an exponential law. Fitting such laws gives a straightforward way to estimate λ_K as a function of the two parameters $\mathcal{F}$ and $\kappa^\star$. The results are shown in figure 7*b*.

One finds that when $\mathcal{F}$ is large enough, all data indeed collapse when represented as a function of the non-dimensional parameter $(1/\mathcal{F})\,\log(\kappa^\star/\kappa_0)$.

To propose fitting formulae for this rate, we rely on approximating the distribution of turbulent velocity gradients by either a stretched exponential or a lognormal law, as was done for tensile failure. In the first case, we write

$$\lambda_K(\kappa^\star) \approx \lambda_0 \exp\left[-a\left(\frac{\log(\kappa^\star/\kappa_0)}{\mathcal{F}}\right)^{1/2}\right], \tag{4.12}$$

with fitting parameters λ_0 (with the dimension of a frequency) and a (dimensionless). As can be seen in figure 7*a*, this a formula gives a rather good approximation. As to the lognormal fit, it reads

$$\lambda_K(\kappa^\star) \approx \lambda_0' \exp\left[-a'\left[\log\left(\frac{\log(\kappa^\star/\kappa_0)}{\mathcal{F}}\right)+b'\right]^2\right], \tag{4.13}$$

where the fitting parameters are this time a frequency λ_0' and two dimensionless parameters a' and b'. As for tension, the lognormal fit does not describe well data associated to the tail of the distribution, that is small values of $\mathcal{F}$ or, equivalently, large values of $\kappa^\star$. These two fits provide estimates of the rate at which flexural failure occurs as a function of all physical parameters, including the fibre length, aspect ratio, Young modulus, the fluid velocity and mass density that enter the definition of the non-dimensional flexibility $\mathcal{F}$ given in equation (2.3).

(ii) Daughter size distribution

We next turn our attention to understand the resulting sizes of the fragments obtained due to flexural failure during buckling. Up to now, by focusing on the flexural failure rate, we have addressed only a single (the first) break-up event. Because the fibre is curved according to a given buckling mode of order n, the location where break-up occurs clearly depends on n. When n is is odd, the break-up occurs at the centre of the fibre, which breaks in two equal pieces. When n is even, the two resulting fragments have approximately sizes $\ell \times (n/2)/(n+1)$ and $\ell \times (n/2+1)/(n+1)$. Actually, this primary break-up is sometimes followed by successive fragmentations. We indeed find that, because of the continuing compression by the flow, the unstable mode keeps on bending the small secondary pieces, so that their curvature still grows and can reach again the critical value. This is illustrated for a specific buckling event in figure 8 where we have implemented in the numerical simulation the break-up process and the follow-up of resulting fragments. In this case, the instability triggers the growth of a mode of order $n = 14$ (figure 8*a*). A first break-up occurs at $s \approx -0.02\,\ell$, but the resulting fragments undergo successive fragmentations. This process finally leads to the formation of eight pieces. In this daughter distribution, six fragments have sizes of the order of $\ell/(n+1) \approx 0.07\,\ell$, the two remaining being associated with the ends of the original fibre (figure 8*c*). As can be followed in figure 8*b*, the locations where new break-ups occur follow the structures of the initial bending. Note that the full process occurs on time scales of the order of τ_η, confirming that this corresponds to a single buckling event. Note that for this specific event, we have tested how the fragmentation process depends upon the numerical scheme, and in particular on the choice of the time step size Δt. Our results indicate that stability and convergence are ensured only when Δt is much smaller than the local time scale prescribed by the instability growth rate. In order to maintain a reasonable computational cost, we have thus implemented a time-adaptive strategy that accounts for such a constraint.

A single buckling event can hence lead to the creation of several small pieces, depending on which wavenumber is excited. The selection of the most unstable mode depends on the local value of the non-dimensional flexibility $\mathcal{F}_{\rm loc} = \tau_\eta\,|\dot\gamma|\,\mathcal{F}$, which fluctuates with $\dot\gamma$. Following the results of previous section, we expect for a given value of $\mathcal{F}_{\rm loc}$ that the most unstable mode is of order $n \simeq 2k^\star \simeq \sqrt{\mathcal{F}_{\rm loc}}/(\pi\sqrt{32})$. In that case, the daughter distribution will be peaked at $\ell' = \ell/(n+1) \simeq \pi\sqrt{32}\,\ell/\sqrt{\mathcal{F}_{\rm loc}}$. Assuming that each buckling event leads to break the fibre in $(n+1)$ fragments of equal size ℓ', we can draw an approximation for the daughter size distribution. Hence, the

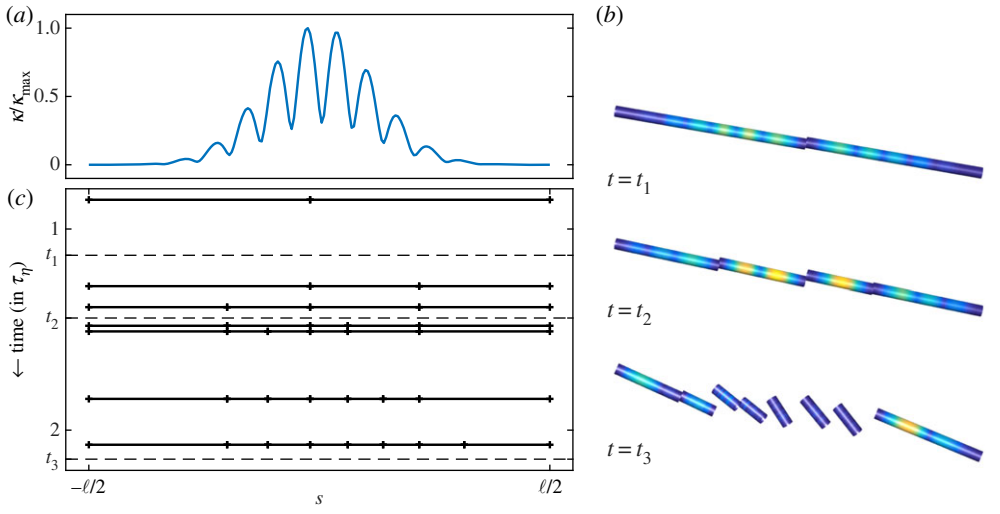

Figure 8. Evolution of a fibre during fragmentation. Panel (*a*) shows the growing mode by displaying, at the time of the first break-up, the fibre's curvature as a function of the arc-length *s*. Panel (*c*) represents the time evolution of the size distribution (time growing from top to down); each horizontal plain line is a break-up event and segments correspond to fibre fragments. (*b*) Three instantaneous configurations of the fragments at time t_1, t_2 and t_3. Dark regions (blue online) correspond to a zero curvature and light (yellow online) to values close to $\kappa^\star$. Note that on this pseudo three-dimensional representation, the arc-length *s* runs from right to left. (Online version in colour.)

probability that a fibre of length ℓ breaks in ℓ/ℓ' fragments of size ℓ' reads

$$\Pr(\ell \to \ell') \propto \frac{\ell/\ell'}{\tau_\eta \mathcal{F}}\; p_{\dot\gamma}\left(-\frac{32\pi^2(\ell/\ell')^2}{\tau_\eta \mathcal{F}}\right), \tag{4.14}$$

where $p_{\dot\gamma}(\cdot)$ denotes the probability density function of the stretching rate $\dot\gamma$. Assuming as previously that the later follows a stretched-exponential law, one obtains

$$\Pr(\ell \to \ell') \propto \frac{\ell/\ell'}{\mathcal{F}}\, \mathrm{e}^{-a\,(\ell/\ell')/\sqrt{\mathcal{F}}}, \tag{4.15}$$

where a is a positive constant. This particularly simple form suggests that the creation of small-length fragments follows an activation-like distribution. In practical terms, this implies that fragment sizes below $a\ell/\sqrt{F}$ are statistically irrelevant and almost never observed. An equivalent form can be written for lognormal statistics of $\dot\gamma$, namely

$$\Pr(\ell \to \ell') \propto \frac{\ell/\ell'}{\mathcal{F}}\, \mathrm{e}^{-a'\left[\log((\ell/\ell')^2/\mathcal{F})+b'\right]^2}, \tag{4.16}$$

with a' and b' constants. This second leads to the same qualitative considerations as above.

Finally, to illustrate the complexity of this process, we show in figure 9, the fibre length distribution of fibres after the first fragmentation series. All fibres have initially the same length ℓ and the same non-dimensional flexibility $\mathcal{F} = 32\,000$. The simulation is done for a specific value of the critical curvature ($\kappa^\star = 10^{-6}\ell^{-1}$), above which these fibres break. A fragmentation series is defined as the set of break-ups occurring during the same buckling event, that is in a time lag going from the initial development of the buckling instability to the time when all fragments have relaxed to a fully straight configuration. The resulting distribution is clearly multi-modal. It develops a peak at sizes ℓ' of the order of $\ell/2$, corresponding to fibres that broke only once during this series. Such events represent approximately one half of the fragmentations. Another marked peak is present at $\ell' \approx \ell/12$. This other maximum is an artefact of the representation, as smaller are the segment, more numerous they are. Clearly, the number of fragments sharply tends to zero

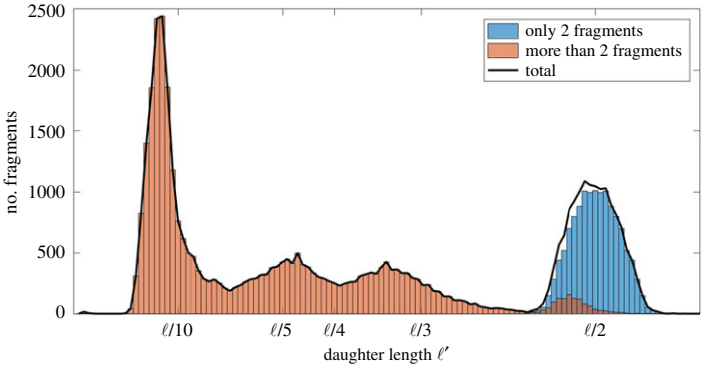

Figure 9. Histogram of the length ℓ' of fragments stemming from the first fragmentation event encountered by 12 000 fibres with initial length ℓ and a flexibility $\mathcal{F} = 320\,000$. (Online version in colour.)

when their size becomes very small. Finally, the distribution displays finite values at intermediate sizes, contributing a significative probability of obtaining fragments of sizes $\ell/3$, $\ell/4$, $\ell/5$, etc.

5. Conclusion and perspectives

We have studied the fragmentation processes undergone by small, inextensible, inertialess fibres in turbulent flow, focusing on tensile and flexural failures. In both cases, we have shown that break-up occurs when the fibre runs into a flow region of high strain, where it is either stretched above internal cohesive forces or compressed, buckles and fractures under excessive bending. By assuming an idealized description for internal fragmentation processes, we found that the fragmentation rates can be expressed through the distribution of turbulent stretching rates. Using standard functional approximations for such probability laws, we proposed fits for both the tensile failure and the flexural failure rates that are calibrated and validated against the results of direct numerical simulations in a high-Reynolds-number flow. Our analysis emphasizes the central role played by the fibres non-dimensional flexibility in understanding how frequently fragmentation occurs.

Besides rates, we reported results on daughter size distributions upon fragmentation. Tensile failure always occurs when the fibre is stretched by the flow and thus has a fully straight configuration. The tension is then maximal at its centre, so that this type of break-up always produces two fragments with equal sizes. We found that the situation is more intricate in the case of flexural failure. Fragmentation occurs when the fibre develops a buckling instability and the resulting break-up process produces a size distribution that depends on the details of the most unstable buckling mode. By performing a linear stability analysis, we provided estimates of this size distribution that depend on the instantaneous fluid strain experienced by the fibre. This approach indicates that the number of fragments produced upon break-up becomes larger when the fibres experiences more violent compressions. Our analysis builds upon the results of Vandenberghe & Villermaux [13] on how buckling affects the fragmentation of elastic slender bodies. Specifically, they studied the fragmentation of elongated bodies considering the effect of inertia (which has been neglected in this paper). They show the existence of an additional effect in the fragmentation process: the propagation of elastic waves after a first break-up. The released energy is able to increase further the curvature in the newly separated parts of the fibre, possibly leading to successive secondary break-ups and to the formation of many small-size fragments. In our work, we unveil another, possibly complementary mechanism where the smaller fragments appear as fingerprints of the initial most-unstable growing mode. The case of inertial fibres with a size that can be larger than the Kolmogorov scale will be studied in the future.

An appealing prospective to our work concerns the Reynolds-number dependence of fragmentation rates and processes. While our numerics limited themselves to a single level of turbulence, our analysis can be easily extended to encompass intermittent descriptions of turbulent statistics. At a qualitative level, one expects more violent fluctuations as the Reynolds number increases. This implies that the rare events leading to the production of many small fragments should have an increasing statistical relevance. At a quantitative level, one can for instance apply the recent work of Buaria *et al.* [34], who carefully investigated the Reynolds-number dependence of the probability distributions of velocity gradients. Their findings can be straightforwardly used in our approach to write an explicit Reynolds-number dependence of the fragmentation rates and associated daughter size distributions.

Finally, it is important to stress again that, in this work, we have oversimplified the microscopical break-up processes by considering that the fibres material is brittle and that fibres are free of any molecular defects. In most realistic settings, the threshold value for each break-up mechanism may vary along the fibre length while plastic effect cannot be neglected, meaning that flexural failure may occur at locations that have been bended several times in the fibre's history. Even if they involve an extra parametrization, such effects can be easily implemented and investigated numerically (e.g. [40]). We expect in particular interesting impacts of the non-trivial time distribution of violent fluctuations. The turbulent fluid strain that is experienced by a fibre along its Lagrangian trajectory is typically very intermittent in time, so that buckling events are strongly correlated among each other. Nevertheless, generalizing to such settings the analysis that has been developed here represents a real challenge. The strongest bending is indeed expected to occur when the buckling instability has saturated, questioning in that case the relevance of the linear analysis. Besides, the more general case of prolate/oblate particles with a finite aspect ratio requires more subtle fragmentation scenario since it can occur along two-dimensional planes, leading to fragments that can quickly display a more complex shape.

Data accessibility. The data that support the findings of this study are available from the corresponding author on request.

Authors' contributions. S.A. carried out the numerics. S.A. and J.B. performed the data analysis. J.B. and C.H. conceived and designed the study. S.A., J.B. and C.H. drafted the manuscript. All authors read and approved the manuscript.

Competing interests. The authors declare that they have no competing interests.

Funding. This work was performed using HPC resources from GENCI-TGCC (grant no. t2016-2as027). S.A. has been supported by EDF R&D (projects PTHL of MFEE and VERONA of LNHE) and by the French government, through the Investments for the Future project UCA^{JEDI} ANR-15-IDEX-01 managed by the Agence Nationale de la Recherche.

Acknowledgements. We acknowledge H. Homann and C. Siewert for their essential help with the numerical simulations, as well as G. Verhille and B. Favier for discussions.

References

1. Beysens D, Campi X, Pefferkorn E. 1995 *Fragmentation phenomena*. Singapore: World Scientific.
2. Hüfner J, Mukhopadhyay D. 1986 Fragmentation of nuclei, stones and asteroids. *Phys. Lett. B* **4**, 373–376. (doi:10.1016/0370-2693(86)90397-7)
3. Nagata S. 2000 Apoptotic DNA fragmentation. *Exp. Cell Res.* **256**, 12–18. (doi:10.1006/excr.2000.4834)
4. Yan B *et al.* 2006 A unique role of the DNA fragmentation factor in maintaining genomic stability. *Proc. Natl Acad. Sci. USA* **103**, 1504–1509. (doi:10.1073/pnas.0507779103)
5. Keil K, Haack H, Scott ERD. 1994 Catastrophic fragmentation of asteroids: evidence from meteorites. *Planet. Space Sci.* **42**, 1109–1122. (doi:10.1016/0032-0633(94)90011-6)
6. Seames WS. 2003 An initial study of the fine fragmentation fly ash particle mode generated during pulverized coal combustion. *Fuel Proc. Tech.* **81**, 109–125. (doi:10.1016/S0378-3820(03)00006-7)

7. Verawaty M, Tait S, Pijuan M, Yuan Z, Bond PL. 2013 Breakage and growth towards a stable aerobic granule size during the treatment of wastewater. *Water Res.* **47**, 5338–5349. (doi:10.1016/j.watres.2013.06.012)
8. Griffith L. 1943 A theory of the size distribution of particles in a comminuted system. *Can. J. Res.* **21**, 57–64. (doi:10.1139/cjr43a-005)
9. Horn AF, Merrill EW. 1984 Midpoint scission of macromolecules in dilute solution in turbulent flow. *Nature* **312**, 140–141. (doi:10.1038/312140a0)
10. Åström JA. 2006 Statistical models of brittle fragmentation. *Adv. Phys.* **55**, 247–278. (doi:10.1080/00018730600731907)
11. Babler MU, Biferale L, Lanotte AS. 2012 Breakup of small aggregates driven by turbulent hydrodynamical stress. *Phys. Rev. E* **85**, 025301. (doi:10.1103/PhysRevE.85.025301)
12. Rösler J, Harders H, Baeker M. 2007 *Mechanical behaviour of engineering materials: metals, ceramics, polymers, and composites*. Berlin, Germany: Springer.
13. Vandenberghe N, Villermaux E. 2013 Geometry and fragmentation of soft brittle impacted bodies. *Soft Matter* **9**, 8162–8176. (doi:10.1039/c3sm50789k)
14. Lundell F, Söderberg L, Alfredsson P. 2011 Fluid mechanics of papermaking. *Annu. Rev. Fluid Mech.* **43**, 195–217. (doi:10.1146/annurev-fluid-122109-160700)
15. Ardekani N, Sardina G, Brandt L, Karp-Boss L, Bearon RN, Variano EA. 2017 Sedimentation of inertia-less prolate spheroids in homogenous isotropic turbulence with application to non-motile phytoplankton. *J. Fluid Mech.* **831**, 655–674. (doi:10.1017/jfm.2017.670)
16. Santoso A, Ilmi B. 2018 Analysis of erosion rate on discharge slurry HDPE pipe in canal water intake PLTGU Grati using CFD simulation. *Int. J. Marine Eng. Innov. Res.* **2**, 253–260. (doi:10.12962/j25481479.v2i4.4063)
17. Becker L, Shelley M. 2001 Instability of elastic filaments in shear flow yields first-normal-stress differences. *Phys. Rev. Lett.* **87**, 198301. (doi:10.1103/PhysRevLett.87.198301)
18. Lindner A, Shelley M. 2016 Elastic fibers in flows. In *Fluid-structure interactions in low-Reynolds-number flows* (eds C Duprat, H Stone), ch. 5, pp. 168–192. Cambridge, UK: The Royal Society of Chemistry. (doi.org/10.1039/9781782628491-00168).
19. Biferale L, Meneveau C, Verzicco R. 2014 Deformation statistics of sub-Kolmogorov-scale ellipsoidal neutrally buoyant drops in isotropic turbulence. *J. Fluid Mech.* **754**, 184–207. (doi:10.1017/jfm.2014.366)
20. Ray SS, Vincenzi D. 2018 Droplets in isotropic turbulence: deformation and breakup statistics. *J. Fluid Mech.* **852**, 313–328. (doi:10.1017/jfm.2018.453)
21. Kobayashi M, Adachi Y, Ooi S. 1999 Breakup of fractal flocs in a turbulent flow. *Langmuir* **15**, 4351–4356. (doi:10.1021/la980763o)
22. Vanapalli SA, Ceccio SL, Solomon MJ. 2006 Universal scaling for polymer chain scission in turbulence. *Proc. Natl Acad. Sci. USA* **103**, 16 660–16 665. (doi:10.1073/pnas.0607933103)
23. Pereira AS, Soares EJ. 2012 Polymer degradation of dilute solutions in turbulent drag reducing flows in a cylindrical double gap rheometer device. *J. Non-Newtonian Fluid Mech.* **179**, 9–22. (doi:10.1016/j.jnnfm.2012.05.001)
24. Odell JA, Keller A. 1986 Flow-induced chain fracture of isolated linear macromolecules in solution. *J. Polym. Sci.* **24**, 1889–1916. (doi:10.1002/polb.1986.090240901)
25. Allende S, Henry C, Bec J. 2018 Stretching and buckling of small elastic fibers in turbulence. *Phys. Rev. Lett.* **121**, 154501. (doi:10.1103/PhysRevLett.121.154501)
26. Domokos G, Kun F, Sipos AA, Szabó T. 2015 Universality of fragment shapes. *Sci. Rep.* **5**, 9147. (doi:10.1038/srep09147)
27. Homann H, Dreher J, Grauer R. 2007 Impact of the floating-point precision and interpolation scheme on the results of DNS of turbulence by pseudo-spectral codes. *Comput. Phys. Commun.* **177**, 560–565. (doi:10.1016/j.cpc.2007.05.019)
28. Tornberg A, Shelley M. 2004 Simulating the dynamics and interactions of flexible fibers in Stokes flows. *J. Comput. Phys.* **196**, 8–40. (doi:10.1016/j.jcp.2003.10.017)
29. Grady D. 2010 Length scales and size distributions in dynamic fragmentation. *Int. J. Fracture* **163**, 85–99. (doi:10.1007/s10704-009-9418-4)
30. Chevillard L, Roux SG, Lévêque E, Mordant N, Pinton J-F, Arnéodo A. 2003 Lagrangian velocity statistics in turbulent flows: effects of dissipation. *Phys. Rev. Lett.* **91**, 214502. (doi:10.1103/PhysRevLett.91.214502)
31. Kailasnath P, Sreenivasan KR, Stolovitzky G. 1992 Probability density of velocity increments in turbulent flows. *Phys. Rev. Lett.* **68**, 2766. (doi:10.1103/PhysRevLett.68.2766)

32. Meneveau C, Sreenivasan K R. 1991 The multifractal nature of turbulent energy dissipation. *J. Fluid Mech.* **224**, 429–484. (doi:10.1017/S0022112091001830)
33. Donzis DA, Yeung PK, Sreenivasan KR. 2008 Dissipation and enstrophy in isotropic turbulence: resolution effects and scaling in direct numerical simulations. *Phys. Fluids* **20**, 045108. (doi:10.1063/1.2907227)
34. Buaria D, Pumir A, Bodenschatz E, Yeung PK. 2019 Extreme velocity gradients in turbulent flows. *New J. Phys.* **21**, 043004. (doi:10.1088/1367-2630/ab0756)
35. Jeffery GB. 1922 The motion of ellipsoidal particles immersed in a viscous fluid. *Proc. R. Soc. Lond. A* **102**, 161–179. (doi:10.1098/rspa.1922.0078)
36. Munk T, Hallatschek O, Wiggins CH, Frey E. 2006 Dynamics of semiflexible polymers in a flow field. *Phys. Rev. E* **74**, 041911. (doi:10.1103/PhysRevE.74.041911)
37. Subramanian G, Koch DL. 2005 Inertial effects on fibre motion in simple shear flow. *J. Fluid Mech.* **535**, 383–414. (doi:10.1017/S0022112005004829)
38. Einarsson J, Candelier F, Lundell F, Angilella JR, Mehlig B. 2015 Rotation of a spheroid in a simple shear at small Reynolds number. *Phys. Fluids* **27**, 063301. (doi:10.1063/1.4921543)
39. Bender CM, Orszag SA. 1999 *Advanced mathematical methods for scientists and engineers I: asymptotic methods and perturbation theory*. New York, NY: Springer.
40. Marchioli C, Soldati A. 2015 Turbulent breakage of ductile aggregates. *Phys. Rev. E* **91**, 053003. (doi:10.1103/PhysRevE.91.053003)